

Article

# Prediction of Crosswind Separation Velocity for Fan and Nacelle Systems Using Body Force Models: Part 2: Comparison of Crosswind Separation Velocity with and without Detailed Fan Stage Geometry

Quentin J. Minaker and Jeffrey J. Defoe \* 

Turbomachinery and Unsteady Flows Research Group, Department of Mechanical, Automotive, and Materials Engineering, University of Windsor, 401 Sunset Ave., Windsor, ON N9B 3P4, Canada

\* Correspondence: [jdefoe@uwindsor.ca](mailto:jdefoe@uwindsor.ca); Tel.: +1-(519)-253-3000 (ext. 5961)

Received: 9 October 2019; Accepted: 10 December 2019; Published: 17 December 2019



**Abstract:** Modern aircraft engines must accommodate inflow distortions entering the engines as a consequence of modifying the size, shape, and placement of the engines and/or nacelle to increase propulsive efficiency and reduce aircraft weight and drag. It is important to be able to predict the interactions between the external flow and the fan early in the design process. This is challenging due to computational cost and limited access to detailed fan/engine geometry. In this, the second part of a two part paper, we apply the fan gas path and body force model design process from Part 1 to the problem of predicting flow separation over an engine nacelle lip caused by crosswind. The inputs to the design process are based on NASA Stage 67. A body force model using the detailed Stage 67 geometry is also used to enable assessment of the accuracy of the design process based approach. In uniform flow, the model produced by the design process recreates the spanwise loading distribution of Rotor 67 with a 7% RMS error. Both models are then employed to predict crosswind separation velocity. The two approaches are found to agree in their prediction of the crosswind separation velocity to within 5%.

**Keywords:** fan–nacelle interaction; body force models; turbomachinery; CFD; crosswind; nacelle

## 1. Introduction

Modern aircraft engine design is moving towards using larger bypass ratios with lower fan stagnation pressure ratios. This improves propulsive efficiency; however, it comes with the negative trade off of larger and heavier nacelles. To combat this negative side effect, manufacturers are using shorter inlets with thinner nacelle lips [1]; however, these changes increase the chance of flow separation occurring in the inlet. The airframers' ability to determine the impact of these changes is important during design. To model such situations, the airframer must be able to also model the engine fan stage as its operation will greatly impact the intake performance [1]; however, two major concerns arise while modelling these flows. The first is that it requires full wheel simulations to capture the non-uniform flow caused by inlet separation; using traditional bladed full wheel simulations to model non-uniform flow is very computationally expensive. These bladed full wheel simulations can contain over 100 million cells for the internal flow alone, usually require 20–30 rotor revolutions to obtain statistically stationary results [2,3], and can take over two months to complete even with modern computing power. The second issue is that access to detailed fan stage geometry may not be possible and that most airframers lack the expertise or time required to reproduce this geometry.

The solution to the first issue is to use a simplified model of the propulsion system. This reduces the computational cost, as it allows for steady simulations and reduces the number of cells required.

Godard et al. (2017) [4] discussed multiple simplified modelling approaches and concluded that a body force approach was needed to capture the coupling effect between the external flow and the fan's operation. Body force methods work by applying sources of momentum and energy in the swept volumes where the blades would normally be. Another study conducted by Burlot et al. (2018) [5] compared simplifying methods to high fidelity unsteady Reynolds averaged Navier–Stokes (RANS) simulations of a nacelle casing with non-uniform inflows; it agreed with the findings of Godard et al. (2017) and showed that body force models worked better than other simplifying methods at reproducing the results of the unsteady RANS simulations. The body force method captures radial distributions of stagnation pressure and downstream distortion maps as smeared out averages of that seen in the bladed simulations.

Many variations of the body force method exist; however, they commonly require calibration based on experimental results or detailed bladed simulations. As described in Part 1 of this paper [6], the model produced by Hall et al. (2017) [7] requires no calibration; however, it still requires blade geometry and gas path information. This relates to the second issue mentioned earlier as this information would typically not be available. Part 1 described a process that creates a simplified fan stage gas path and body force model using Hall's method with limited stage information, and it was shown to produce the desired results at design conditions.

In this process, the desired thrust, fan stagnation pressure ratio (*FPR*), and geometric parameters, all of which would commonly be known by an airframer, are inputs used to generate a body force model. The process consists of using 1D analysis through the fan stage, simplified blade camber shapes, and simplifying assumptions to find the required information needed for the Hall body force approach. How the parameters are found, what assumptions are made, and the steps used to create the body force model were described in Part 1 [6].

An important non-uniform flow studied is the crosswind around a nacelle because it is the most likely scenario to result in inlet separation. In Yeung et al. (2019) [8], different nacelles were tested with crosswind flows, and the effects on the separation velocity and the stagnation pressure distributions were described. In Lee et al. (2018) [9], the effect that crosswind had on the operation of the fan stage was analysed. It was found that this inlet distortion caused a loss in stall margin, even in cases where separation had not occurred. The authors also discussed the suppression effect that the fan applied to the inlet separation. These findings further emphasized the importance of designers being able to incorporate this external flow–fan stage interaction into the nacelle design process.

The objective of this paper is to assess the ability of a model produced using the simplified process detailed in Part 1 to predict the crosswind separation velocities seen in a real machine operating with crosswind. The model design process is used to create a gas path and body force model based on a real machine, NASA Stage 67. Both the created stage and the original NASA Stage 67 are run using the body force approach (Hall's model) with varying crosswind speeds, and the results are compared. In Hall et al. (2017) [7], the model's ability to capture upstream flow redistribution and distortion transfer correctly showed good agreement with higher fidelity models. Comparing the results from NASA Stage 67 to those of the simplified stage will allow for a quantification of the accuracy lost by simplifying the stage design. The key outcomes are that the design simplification has minor effects on the rotor and the nacelle performance prediction.

The first section of this paper will discuss how the simplified stage is created. This simplified stage is run at the design condition and compared to the original NASA Stage 67. Next, the numerical setup of the full wheel crosswind simulation is described. In the Results Section, the full wheel crosswind body force simulations using the original NASA Stage 67 and the simplified stage are compared. This includes the difference in separation velocities and the effect on the fan stage performance.

## 2. Simplified Stage Creation

The simplified generation process was used to create a stage based on the performance and geometry of NASA Stage 67. The *FPR* supplied to the simplified design process was found using the

results of NASA Stage 67 running at 70% corrected speed at the design flow coefficient using Hall's model [7] with an added compressibility correction, as described in Part 1 [6]. Normally, the process would not require any prior simulations, but as the intent was to create a stage as similar to NASA Stage 67 as possible, this was done here. The corrected speed of 70% was used as this provided similar tip relative Mach numbers to those seen in modern engine fan stages. The details of the Stage 67 simulation, including the setup, validation, and results can be found in Part 1 [6]. This was found to produce an  $FPR$  of 1.31; this value was then supplied for the simplified design process.

The process described in Part 1 used the desired thrust to determine the required mass flow for the machine; however, in this case, the mass flow from the NASA Stage 67 simulation was used so an objective comparison could be made between the two models. This means that the process was slightly altered such that mass flow was supplied, instead of a desired thrust. This was done by substituting the mass flow rate as opposed to the thrust in the thrust equation,

$$F = \dot{m}(V_{19} - V_{\infty}) + A_{19}(p_{19} - p_{\infty}) \quad (1)$$

where  $F$  is thrust,  $\dot{m}$  is the mass flow rate through the fan,  $V$  is the velocity in the aircraft reference frame,  $A$  is flow area normal to the engine rotational axis, and  $p$  is static pressure. The subscripts represent the quantities at the stations shown in Figure 1. The thrust then became an output of the process, though it was not important in this instance.

The design process required several geometric parameters to be specified to enable the generation of the gas path. In this case, all of the parameters required were found using the Stage 67 geometry and applying simplifications as required. Similar to the  $FPR$ , these parameters could be determined without detailed geometry information; however, Stage 67 data [10] were used here so that a comparison could be made and the effects of simplifying the stage design could be seen. The parameters were generated as follows:

- The inlet rotor tip radius of  $r_{\text{tip}} = 0.255$  m and hub-to-tip ratio of 0.375 were set equal to NASA Rotor 67.
- The simplified process generated constant axial coordinate leading and trailing edge blade profiles. The blade aspect ratios were set such that these axial coordinates were equal to the average axial coordinates of the leading and trailing edge profiles from NASA Stage 67, which gave rotor and stator blade aspect ratios of  $b_R/c_R = 2.53$  and  $b_S/c_S = 2.22$ , respectively.
- The parameter that determined the amount of casing radius change through the rotor was set so that there was an equal decrease in radius between the two machines and was  $Y = 0.04$ .
- The spacing between the blades was set so that the stator leading edge was set at an equal axial coordinate to that in NASA Stage 67 and was  $L_2/c_R = 0.706$ .
- The axial length of the spinner nose was set so that the upstream distance from the rotor leading edge (averaged for NASA Stage 67 case) was equal in both cases and was 94% of the length if the rotor hub slope was continued to zero radius.

A comparison between the original NASA Stage 67 gas path and the gas path generated using the simplified design process is shown in Figure 1. It is clear from the figure that the most significant difference was in the shapes of the spinners. This was due to a constraint of continuity of the hub slope between the rotor and spinner in the stage design process employed. This was one factor that contributed to the differences in the flow field upstream of the rotor, which will be discussed later in the paper.

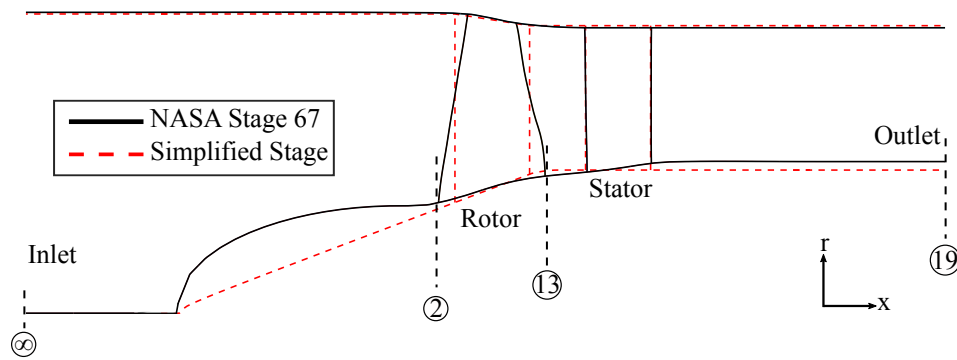


**Figure 1.** Comparison between NASA Stage 67 and simplified stage gas paths and meridional blade profiles.

There was a major difference between the blade shapes and their operation in the NASA Stage 67 compared to the simplified stage. The simplified process generated blade angles at the hub, midspan, and tip. These were used to create a camber surface as described in Part 1 [6]. The change in rotor blade angle from leading to trailing edge found at these spans was  $33.2^\circ$ ,  $7.5^\circ$ , and  $2.3^\circ$ , respectively. The change in blade angles at the same span locations in NASA Stage 67 was  $63.2^\circ$ ,  $17.8^\circ$ , and  $12.2^\circ$ . It was seen that the simplified process generated blades with significantly less turning; however, it created the required overall flow turning by increasing the rotational speed of the blades. The corrected rotational speed of the rotor blades in the simplified stage was 1435 rad/s compared to 1176 rad/s used by NASA Stage 67. This difference in blade shapes was not unexpected or considered an issue though, as the aim was to reproduce stage performance rather than blade shapes. The different rotational speeds implied different velocity triangles and differing local flow characteristics between the two fan models. As will be shown, however, the good agreement in the results obtained using the two models suggested that these effects had only a minor impact on fan upstream influence.

Computational fluid dynamics (CFD) simulations were run with the simplified stage at the design point. A 1/8 slice of the simplified stage was used with uniform inflow, with the same boundary conditions as the NASA Stage 67 simulation used to determine the supplied *FPR* [6]. The grid used contained 559,520 cells and had a distribution similar to what was used by the NASA Stage 67 simulations, and therefore, the grid independence study conducted for NASA Stage 67 in Part 1 was considered sufficient to treat the new results as grid independent. The solver and grid generation tools were the same as those used in Part 1.

#### Comparison of Stages at the Design Condition

The overall performance of the simplified stage was compared against NASA Stage 67 at 70% corrected speed. The simplified stage had a mass averaged fan stagnation pressure ratio (*FPR*-1) of 0.325, which was an 3.83% increase from the desired value of 0.313. In Figure 2, the chordwise and trailing edge spanwise work coefficient,

$$\psi = \frac{h_t - h_{t,\infty}}{U_{\text{mid},67}^2} \quad (2)$$

are compared between the simplified stage and NASA Stage 67, using the blade velocity in NASA Stage 67 for normalisation.  $h_t$  is the stagnation enthalpy, and  $U_{\text{mid},67}$  is the midspan blade speed for Stage 67. The rates of work input in the first 20% chord were generally in good agreement between the two stages across the span, but the overall work input was high for the simplified stage: the spanwise mass averaged work coefficient was 5.15% higher than the target value. The root mean squared (RMS) local difference in work coefficient normalised by the total work addition along the chord at 20%, 50%, and 80% span, as well as at the rotor trailing edge are shown in Table 1. In general, agreement

worsened with increasing span fraction (outside of the endwall regions); however, the trailing edge spanwise profile of work input had only a 7% RMS error, indicating reasonable agreement in overall loading prediction.

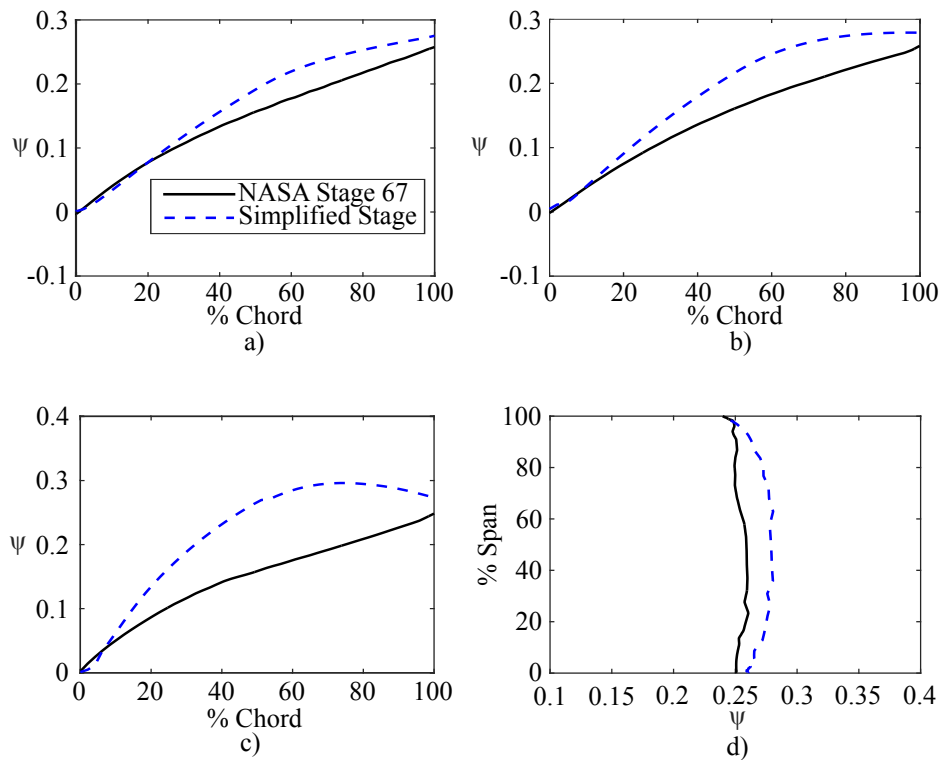


**Figure 2.** Work coefficient vs. meridional distance through the rotor at: (a) 20% span, (b) 50% span, (c) 80% span, and (d) rotor trailing edge.

**Table 1.** Comparison of NASA Stage 67 and the simplified stage.

	RMS Local $\psi$ Error/ $\psi_{TE}$
20% Span	0.091
50% Span	0.147
80% Span	0.284
Spanwise	0.068

The spanwise trailing edge work distribution in the simplified stage had an RMS difference of 2.6% from the mass averaged overall work coefficient for this same case. One of the aims of the design process was to create a spanwise uniform trailing edge work coefficient, and this level of agreement indicated that this had largely been achieved.

A decrease in the accuracy of the actual vs. desired performance was observed for the case shown here compared to the example fan stage studied in Part 1 [6]. The accuracy of *FPR-1* decreased by 2.58%, and the non-uniformity of the spanwise trailing edge work distribution increased by 2%. This decrease in accuracy was primarily caused by the decrease in tip radius through the rotor for the case presented in the current paper. This change caused the axial velocity in the tip region to increase, which led to a radially outward shift in mass flux, as shown in Figure 3; this shift lowered the axial velocity in the midspan region, which modified the velocity triangles all along the span and had the main effect of increasing the work coefficient near midspan.

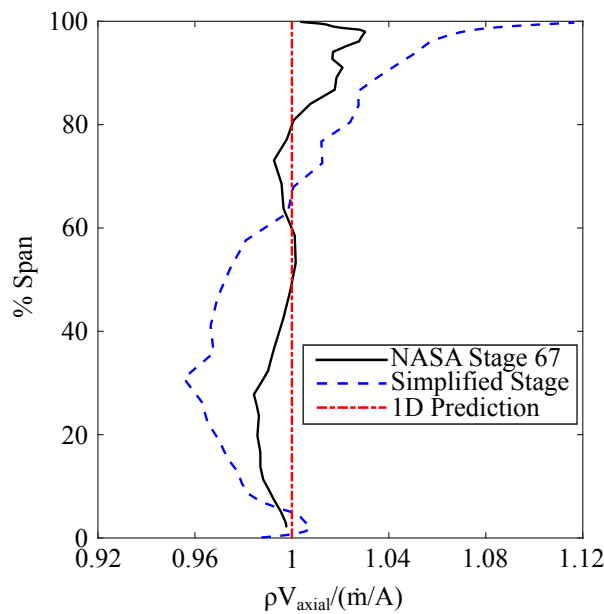


**Figure 3.** Mass flux along the rotor trailing edge.

This simplified stage showed comparable performance to NASA Stage 67 at the selected operating point and therefore provided an adequate foundation to continue with the performance comparison of the two stages with non-uniform inflow.

### 3. Numerical Setup of Full Wheel Crosswind Simulations

The simulations modelled pure crosswind at sea level with no forward movement of the engine/nacelle, similar to the conditions seen at the start of a take-off roll; Ansys CFX v18.2 [11] was used as the solver. The simulations were steady state and used the shear-stress-transport turbulence model [11]. For crosswind velocities, which result in flow separation on the inner part of the nacelle, steady computations provided only an approximate solution to the flow in and downstream of the separated region. If the details of the fan–nacelle interaction were of interest in such cases, then time resolved computations would be more suitable. However, in this paper, we were interested in comparing the ability of the fan models to capture fan–nacelle interaction, and so, the steady treatment was sufficient. In our computations, at even the highest crosswind velocities investigated, the solutions obtained were truly steady, showing good convergence including all fluxes (mass, momentum, and energy) having less than 0.1% imbalance across both the full computational domain and a smaller control volume encompassing just the flow near the nacelle and the internal flow. The computational domain had outer boundaries at 25 engine diameters away from the fan axis, as schematically illustrated in Figure 4. The cylindrical computational domain comprised four separate boundary conditions on its outer surface, since CFX lacks a true far-field boundary condition. The curved surface was divided into two equally sized boundaries, one inlet and one outlet. At the inlet, the static pressure and crosswind velocity were imposed, and the other was an outlet with the same imposed static pressure. The boundaries perpendicular to the fan axis were openings, which in CFX means the boundary can act as either an inlet or an outlet. When the flow left the domain across these boundaries, the static pressure was set to the same value as on the inlet and outlet boundaries. Flow entering across this boundary was treated as total pressure (set as the same value as the static pressure), from which the static pressure was calculated. In these simulations, the static pressure was taken as the sea level standard. A mass flow outlet boundary condition was set at the outlet within the fan stage. The hub and casing curves were set as no slip walls everywhere except downstream of the rotor leading edge, where they switched to zero shear stress walls. This was done as the design

process described in Part 1 made the assumption of zero losses within the turbomachinery and its associated ducting. The spinner nose was a no slip rotating wall with the same rotation speed as the rotor blades. The crosswind velocity was varied.

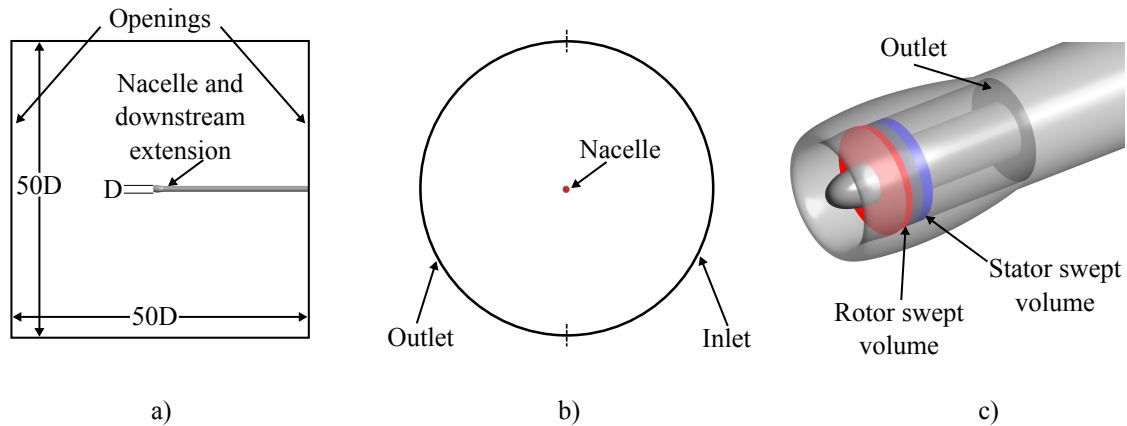


**Figure 4.** Computational domain for crosswind simulations. (a) Side view, (b) front view, and (c) zoomed in view of the nacelle and fan stage.

The nacelle geometry was generated by Bombardier Aerospace for this analysis and was representative of those seen on modern wide body aircraft. Figure 5 shows the meridional profile of the nacelle used. To avoid sharp corners that have been known to cause issues within numerical methods [11], the outside of the nacelle was extended axially outwards to the downstream boundary.

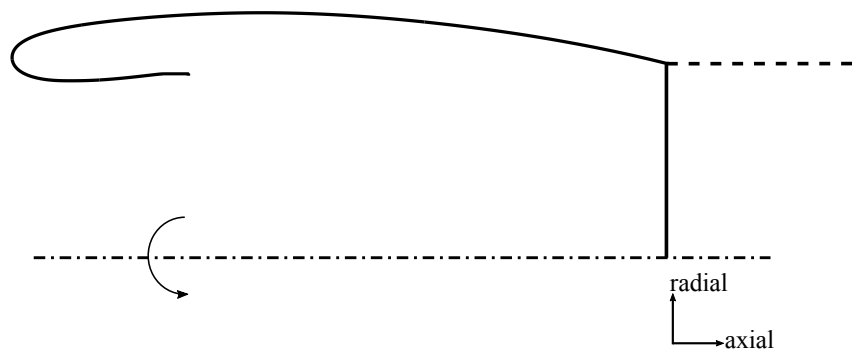


**Figure 5.** Nacelle casing used within full wheel simulations, where the dashed line represents the casing extended axially downstream and the dashed-dotted line is the rotation axis.

An initial structured mesh containing  $13.5 \times 10^6$  nodes was used for the full domain and was generated using Pointwise v18.0 [12]. A cell growth rate of 1.1 was used at all wall boundaries. The grid used downstream of the fan leading edge was similar to that used in the uniform inflow slice from the prior NASA Stage 67 simulations described in Part 1 [6]. The automatic wall treatment option within Ansys CFX v18.2 was used; this treatment was  $y^+$  insensitive; however, it is recommended that at least ten cells exist in the boundary layer if this option is used [11]; this condition was met for all the simulations.

These full wheel simulations were relatively computationally expensive due to larger cell counts (compared to internal flow only computations). This caused two main issues, the first being that the grid independence study itself could become expensive, and the second being that to find the

separation point, many iterations on the crosswind velocity may be necessary. To maintain a lower computational cost, the method presented by Roache [13], which was based on the use of Richardson extrapolation, could be used to determine the expected error based on the grid used. This method involves performing two or more simulations with successively finer grids and assumes that the change in the results should asymptotically approach zero as the number of grid points tends towards infinity.

Three grid levels were assessed for the simplified stage with  $U^* = 0.232$ , where  $U^*$  is the ratio between the crosswind velocity and mass averaged fan leading edge axial velocity. A formal definition of  $U^*$  is provided in the next section. One grid was finer than the one described earlier, and one was coarser.  $U^* = 0.232$  was selected as it was large enough to generate flow separation, but low enough that the flow reattached before the rotor leading edge. The variables of interest in the grid study were the separation size (defined by the percentage of area between the nacelle lip and the rotor leading edge where the shear stress was less than zero in the axial direction) and  $FPR$ . Figure 6 shows these parameters at the three grid levels tested, along with the value predicted using Richardson extrapolation with an infinite number of grid points. The extrapolations predicted a separation size of 3.96% with a possible error of  $\pm 0.06\%$  and an  $FPR$  of 1.308 with a possible error of  $\pm 0.0004$  when the cell count tended to infinity. To maintain lower computational cost, the medium grid level was selected. Therefore, the expected errors in separation size and  $FPR$  between this grid and the values that would be obtained with an infinite grid resolution were  $0.91\% \pm 0.06\%$  and  $0.0004 \pm 0.0004$ , respectively.

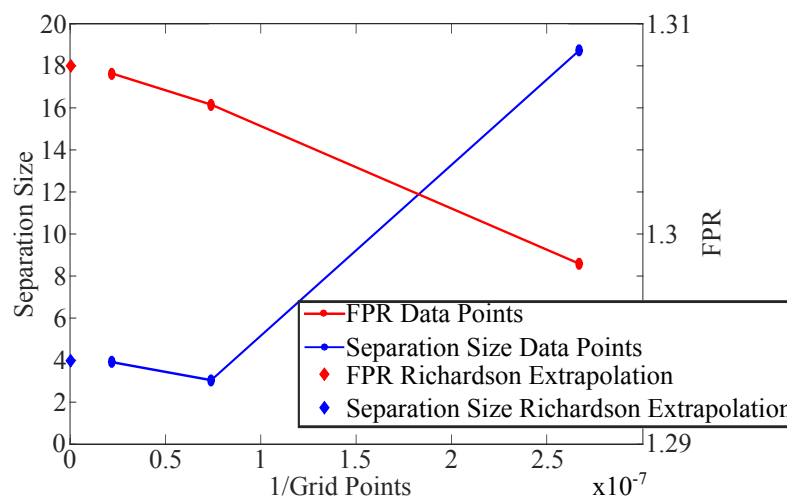


**Figure 6.** Separation size and  $FPR$  as a function of the grid points used to assess error caused by the use of a finite grid size.

#### 4. Results and Discussion of Crosswind Simulations

The crosswind velocity was increased until separation was observed. We define the non-dimensional crosswind velocity to be:

$$U^* = \frac{V_y}{\bar{V}_{x,2}^M} \quad (3)$$

where  $V_y$  is the crosswind velocity and  $\bar{V}_{x,2}^M$  is the mass averaged axial velocity at the fan face (Station 2). Since discrete crosswind velocities are required in CFD, identifying the precise velocity required for separation was challenging. Instead, we aimed to find the value of  $U^*$  to within  $\pm 0.005$  of the value at which separation first occurred. Due to possible hysteresis in the behaviour of the computations, we always moved in the direction of increasing crosswind velocity from one computation to the next. With the conditions tested, the mass averaged axial velocity at the fan face was approximately constant, which translated to a precision of roughly 0.5 m/s for the crosswind velocity.

Flow separation was identified by a region where the flow was locally travelling upstream; this could be identified by a negative value of the wall shear stress in the axial direction on the inside of the nacelle. The point where separation first occurred in NASA Stage 67 was at  $U^* = 0.22$ . The same condition occurred at a value of 0.23 in the simplified stage. This translated to approximately a difference in crosswind velocity of 1.5 m/s between the two stages (5.13% increase). It was possible that the actual difference was smaller since the difference in these two values was not much larger than the possible error due to the discrete values of  $U^*$  assessed. The difference stems from the facts that the simplified stage produced a slightly larger  $FPR$ , that there were differences in the local characteristics of the two fans, and that the spinner shapes for the two machines were different. At this condition, the separation occurred over a short region before the flow reattached. The crosswind velocity was increased further until the flow remained separated up to the fan face within the NASA Stage 67 case; this occurred at  $U^* = 0.30$ . In Figure 7, a  $180^\circ$  slice of the inner nacelle casing is unwrapped and shows the regions of separation at the conditions described here, as well as when the flow is fully attached ( $U^* = 0.21$ ) for both stages.

The regions of separated flow were similar between the two stages. The largest difference when comparing separation was seen in the highly separated case. For NASA Stage 67, the flow separated and remained separated until the fan face; however, in the simplified stage, the flow reattached slightly before the fan face. This occurred for the same reasons as the delayed separation: the slightly larger  $FPR$  created by the simplified stage provided additional suction, which gave rise to a more favourable pressure gradient (aiding flow reattachment), as well as the different local flow characteristics of the fan models and varying meridional velocity distributions caused by different spinner shapes. These effects were also responsible for other differences between the two stages' performance with crosswind, as will be discussed later in this section.

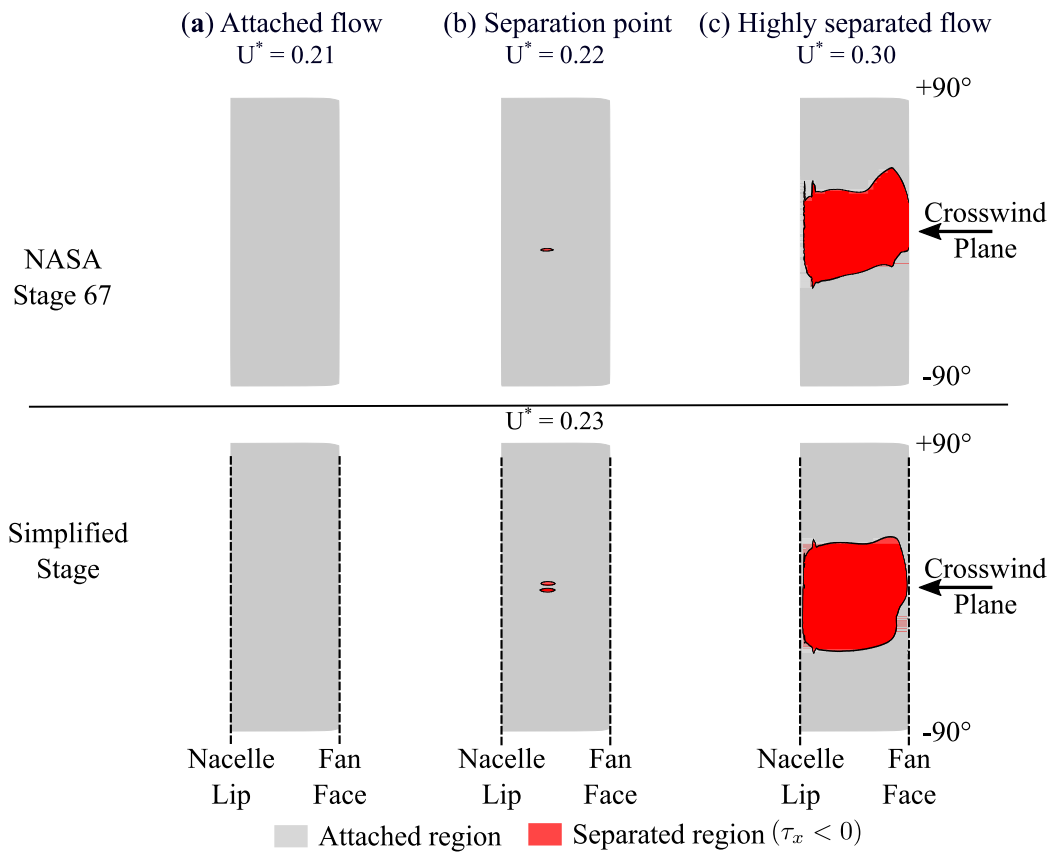


**Figure 7.** Areas of separated flow within the nacelle at the (a) fully attached condition, (b) separation point, and (c) highly separated condition.

Figure 8 shows the contours of the Mach number on a plane tangent with the crosswind direction (and passing through the fan axis) for increasing crosswind velocities. In the attached flow case, the effects of the crosswind were apparent with larger flow acceleration around the nacelle lip followed by a decrease along the nacelle wall. In the highly separated case, the low Mach number region increased in thickness and represented an area of recirculating flow, as shown by the streamlines. The effect of the simplified stage's larger *FPR* and altered characteristic slope was seen in the decreased thickness and axial length of the recirculating region along the nacelle wall. In the highly separated flow case, the radial thickness of the recirculating flow region decreased by 15.4%, and the axial length decreased by 12.2% for the simplified stage.

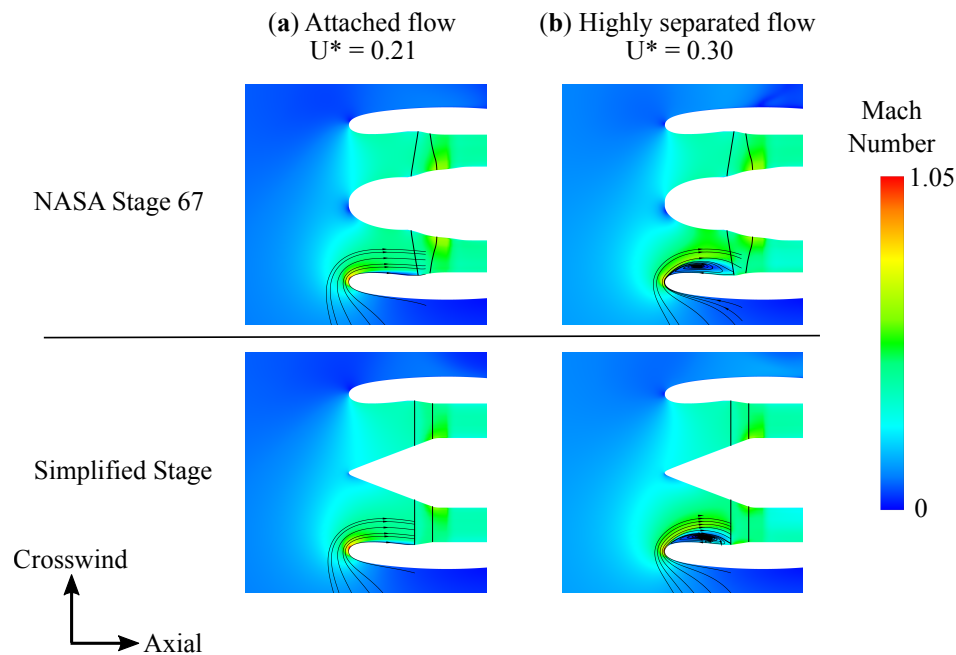


**Figure 8.** Mach number in the plane tangent to crosswind velocity with (a) attached flow and (b) highly separated flow.

The effect of this flow separation at the rotor leading edge was investigated next. Separation caused a decrease in stagnation pressure, which was convected downstream to the rotor. In Figure 9, the ratio of local stagnation pressure to freestream stagnation pressure is shown at the fan leading edge for both stages in the attached and highly separated flow conditions. In Frame (a), the stagnation pressure distribution was mostly uniform, except within the region adjacent to the wall surfaces due to boundary layer losses, which was larger on the side of crosswind flow. In both stages, the maximum radial thickness of the distortion region ( $P_t/P_{t,atm} < 1$ ) was increased by approximately 6% on the side of crosswind flow. The increase in thickness of the distortion region was relatively small and indicated that the flow was fully attached by the fan leading edge and that the crosswind did not have a large adverse effect on fan performance, as will be confirmed later. In Frame (b), the stagnation pressure dropped due to the large separation. The difference in the minimum fan leading edge stagnation pressure between the two stages in the highly separated case was 3.4%, with the larger drop in stagnation pressure being in NASA Stage 67. The two stages showed similar stagnation pressure distributions, with the location of the minimum stagnation pressure at 5.8% span closer to the casing for NASA Stage 67.

To determine the impact of the flow separation on the fan rotor, we next accessed mass flux distributions at the fan leading edge. Figure 10 compares the mass flux distributions at the fan face for both stages in the fully attached condition, as well as the highly separated condition. At  $U^* = 0.21$ , the mass distribution was relatively uniform with a slight decrease along the walls as the velocity went

to zero, which caused a small increase in mass flux near midspan. However, in the highly separated flow case, there were larger differences in the mass flux deviations for the two stages. In the regions of separation, the mass flux was decreased as there was flow recirculation/reversal; this had the effect of causing the adjacent regions to have increased mass flux as the flow accelerated around the edges of the recirculating regions. This was apparent in the NASA Stage 67 case, where the flow recirculation reached the fan (seen as a negative value in the contour plot), and a large increase was seen surrounding this region. The reason behind the slight drop in prediction performance in the highly separated case was due to the simplified stage experiencing flow reattachment slightly before the fan. This indicated that the simplified stage fan had a larger corrective effect on the distribution of mass flux, which stemmed from it having a larger *FPR*, and also possibly steeper loading in the outer span.

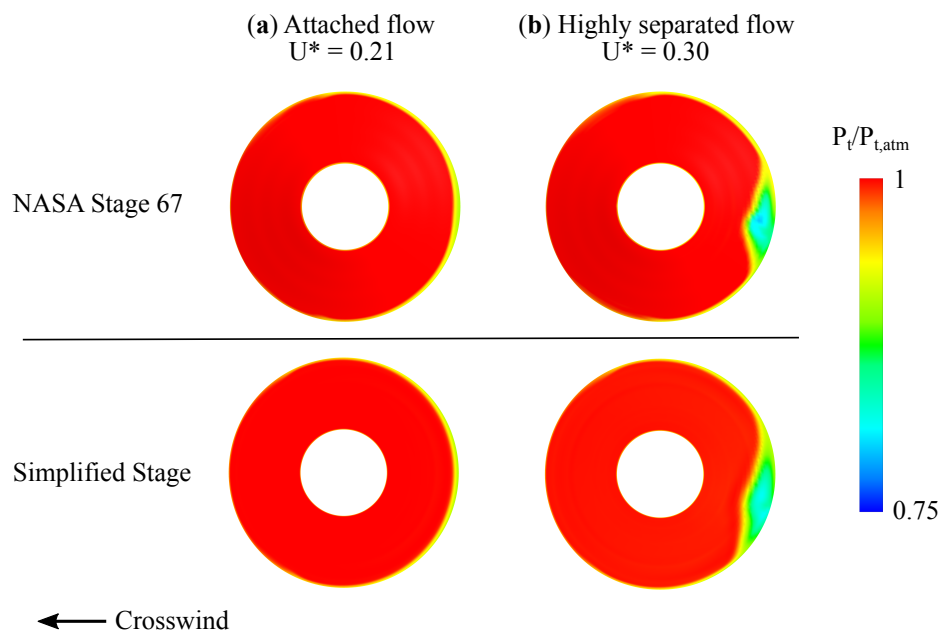


**Figure 9.** Stagnation pressure ratio at rotor leading edge with (a) attached flow and (b) highly separated flow.

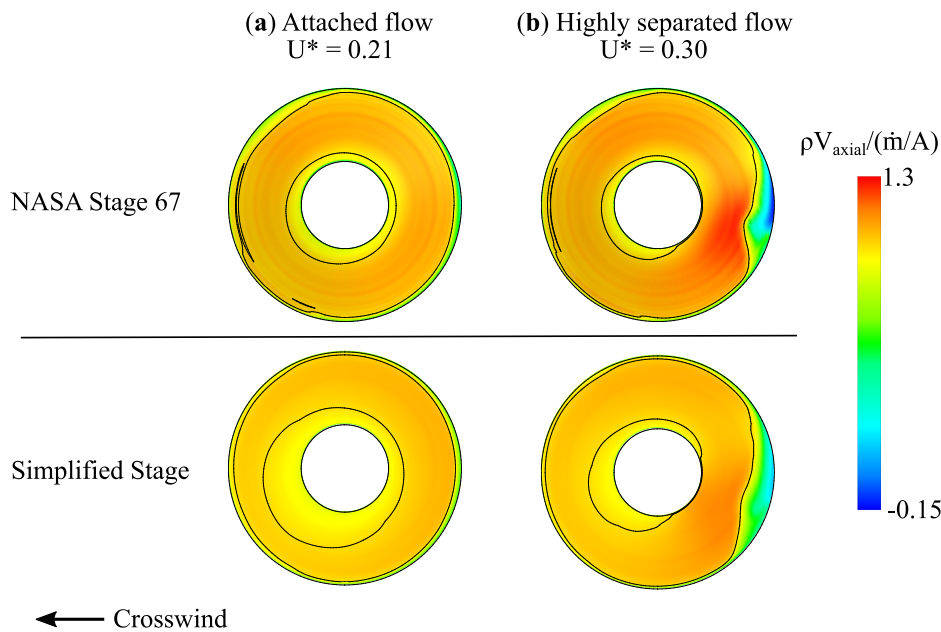


**Figure 10.** Mass flux distribution at the fan face for the (a) fully attached condition and (b) highly separated condition. Isolines of  $\rho V_{\text{axial}} / (\dot{m}/A) = 1$  also shown in black.

To further examine the effects that the separation had on the performance on the fan stage, as well as how accurately the simplified stage captured this, the absolute flow angles and changes in incidence angles were investigated at the rotor leading edge. In Figure 11, the absolute flow angles,  $\alpha$ , are shown along the 20%, 50%, and 80% span lines at the rotor leading edge for both stages in the attached ( $U^* = 0.21$ ) and separated conditions ( $U^* = 0.30$ ). In the attached case, the maximum and minimum flow angles were  $-3.4^\circ$  and  $5.7^\circ$ ; this confirmed that the flow was largely uniform as there were only small changes in flow angles as seen both around the annulus and along the span. The maximum difference in the absolute flow angle between the two stages was  $0.92^\circ$ ,  $1.8^\circ$ , and  $3.2^\circ$  at the 20%, 50%, and 80% span lines, respectively. In the separated case, the absolute flow angles had larger fluctuations in the separated region. The maximum and minimum flow angles were  $20.6^\circ$  and  $-14.9^\circ$ , and these occurred along the 80% span line, as expected, as this travelled through the region directly affected by the separation. The maximum difference in the absolute flow angles at the 20% and 50% span fractions was  $3.4^\circ$  and  $3.3^\circ$ . A maximum difference of  $23.0^\circ$  in the absolute flow angle was seen along the 80% span line at  $\theta = 20^\circ$ ; the reason for this large difference was due to the distortion region being extended over a slightly larger  $\theta$  range. However, the value of the maximum flow angle was in good agreement between the two stages even at 80% span.

Equally important to consider is the incidence, as high incidence can lead to premature stall when it occurs near the tip of the fan blades [9]. In Figures 12 and 13, the changes in incidence angle,  $i$ , from the incidence angle with no crosswind,  $i_{U^*=0}$ , are shown. The comparison to incidence with no inlet distortion, as opposed to using the circumferential variations in incidence, allowed for the effect of operating at an off-design condition (crosswind) to be more clearly seen. In Figure 12, the change in incidence angle for the simplified stage is calculated using the absolute flow angles and the meridional velocity (plotted in Figure 14 normalised by blade speed) produced by the simplified stage CFD simulations; however, the rotational speed used to transform the flow to the relative frame was that of NASA Stage 67. The opposite is true for Figure 13: here, the relative flow angles are determined using the simplified stage's rotational speed for both machines. This approach allowed for a direct comparison of how simplifying the stage affected the prediction of changes in incidence due to the crosswind for a real machine. The incidence further confirmed the earlier observations: that the fan was largely unaffected at the attached condition even with significant crosswind ( $U^* = 0.21$ ), as the change

in incidence was no more than  $+0.3^\circ / -2.3^\circ$  anywhere (for either reference rotational speed). Incidence changes were heavily affected in the regions of separated flow at  $U^* = 0.30$ : for Stage 67 at 80% span, the peak incidence was  $14.3^\circ$  based on Stage 67 rotational speed;  $12.1^\circ$  based on the simplified fan rotational speed. The simplified stage captured the locations of the maximum excursions in incidence and was able to predict the largest reduction in incidence to within  $0.3^\circ$  regardless of the reference rotational speed. The simplified stage under-predicted the maximum increased incidence at 80% span by  $4.8^\circ / 3.8^\circ$  (Stage 67/simplified fan rotational speeds, respectively). While this was a significant difference, the peak incidence for the simplified fan (using its own rotational speed) was still  $8.3^\circ$ . Such a large increase in incidence would almost certainly initiate stall in an actual fan rotor, though the circumferential region over which this occurred was relatively small and would most likely result in decay of the stall cell before it could fully travel around the annulus. Thus, while the simplified fan stage provided only an estimate of the peak incidence associated with the inlet distortion, it still indicated that a problem may exist for rotor operability. Since the simplified modelling approach was intended for use at the preliminary design stage, this was adequate to flag a potential issue that should be investigated with higher fidelity methods once the detailed fan geometry is known.

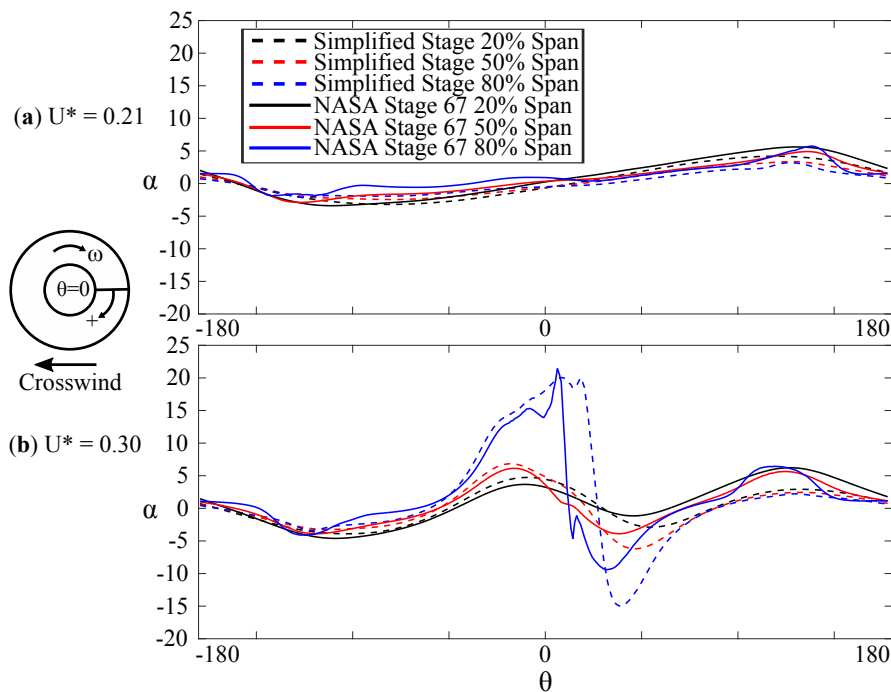


**Figure 11.** Absolute flow angles at the fan leading edge for the (a) fully attached condition and (b) highly separated condition.

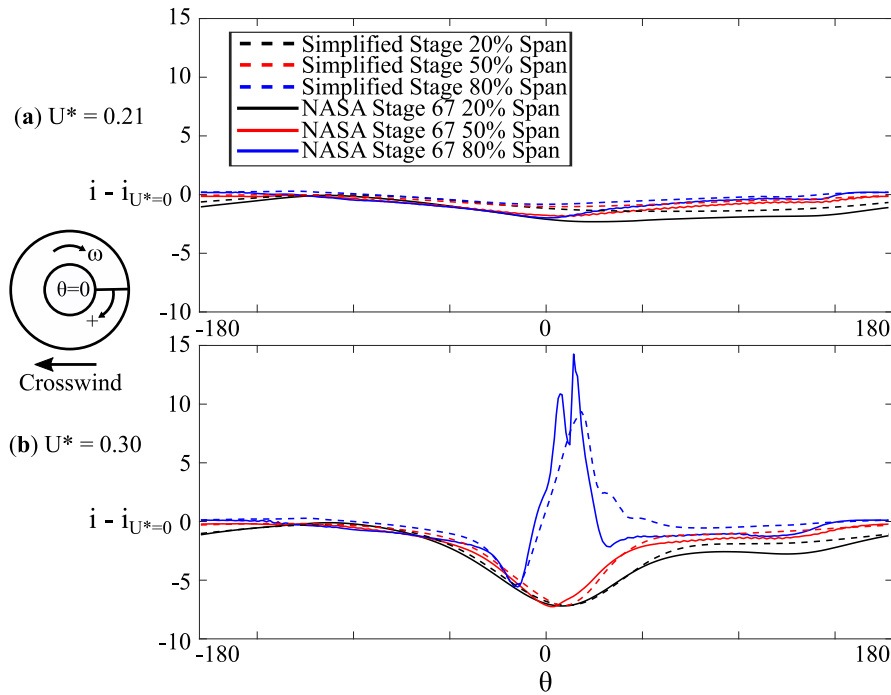


**Figure 12.** Change in incidence angles from the design at the fan leading edge for the (a) fully attached condition and (b) highly separated condition. Relative frame moving at the rotational speed of Stage 67.

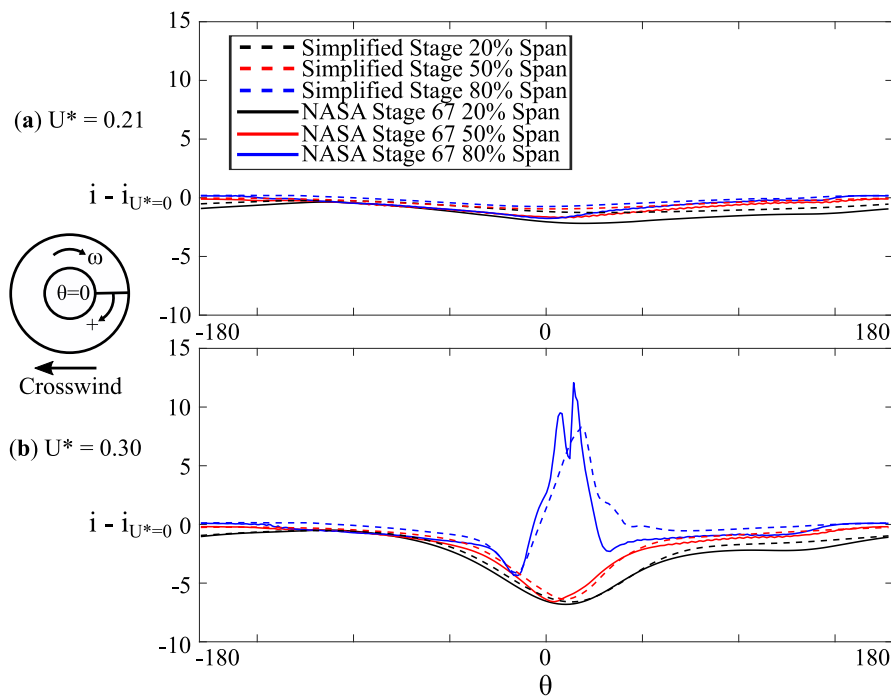


**Figure 13.** Change in incidence angles from the design at the fan leading edge for the (a) fully attached condition and (b) highly separated condition. Relative frame moving at the rotational speed of the simplified fan.

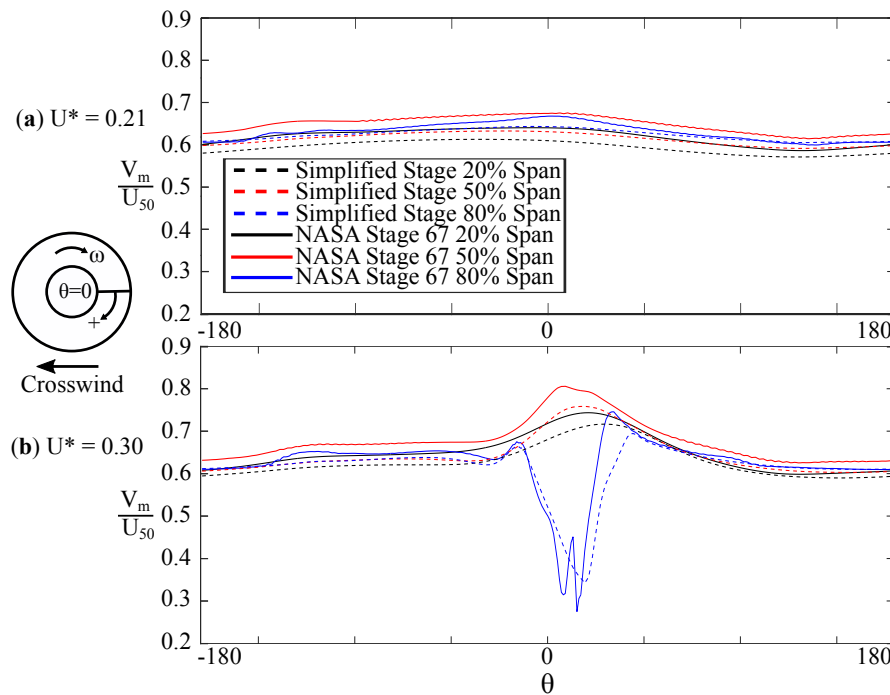


**Figure 14.** Meridional velocity normalised by the blade rotation speed at 50% span at the fan leading edge for the (a) fully attached condition and (b) highly separated condition.

For airframers, it is important to be able to measure the performance of a nacelle. To quantify the performance, the metric known as *DC60* is commonly used [8,9] and is defined as:

$$DC60 = \frac{\bar{p}_{t,60}^A - \bar{p}_t^A}{\bar{p}_t^A - \bar{p}^A} \tag{4}$$

where  $\bar{p}_t$  and  $\bar{p}^A$  are the area averaged stagnation and static pressures at the fan leading edge and  $\bar{p}_{t,60}^A$  is the lowest value of area averaged stagnation pressure over any 60° circumferential sector at the fan leading edge. *DC60* is a measure of inlet distortion and decreases as the fan leading edge separation increases. Though normally mass weighted averages are more meaningful than area weighted ones, use of area weighting is explicit in the common definitions of *DC60*, so we retained that approach here. The *DC60* values, as well as their corresponding circumferential locations are shown in Table 2 for  $U^* = 0.21$  and  $U^* = 0.30$ . In Figure 15, the absolute values of *DC60* as  $U^*$  varies are shown for both stages. Note that an additional computation was carried out at  $U^* = 0.26$ , but since the separation did not extend to the fan leading edge for that case, the results were used only to initialize the solutions at  $U^* = 0.30$ . Thus, this case was not fully run to convergence, so no *DC60* values can be reported.

**Table 2.** *DC60* values for crosswind velocities just before separation and with strong separation.

	NASA Stage 67	Simplified Stage
$DC60_{U^*=0.21}$	−0.0583	−0.0479
$\theta_{U^*=0.21}$ Range (degrees)	−32 to 28	−31 to 29
$DC60_{U^*=0.30}$	−0.3461	−0.3776
$\theta_{U^*=0.30}$ Range (degrees)	−25 to 35	−19 to 41

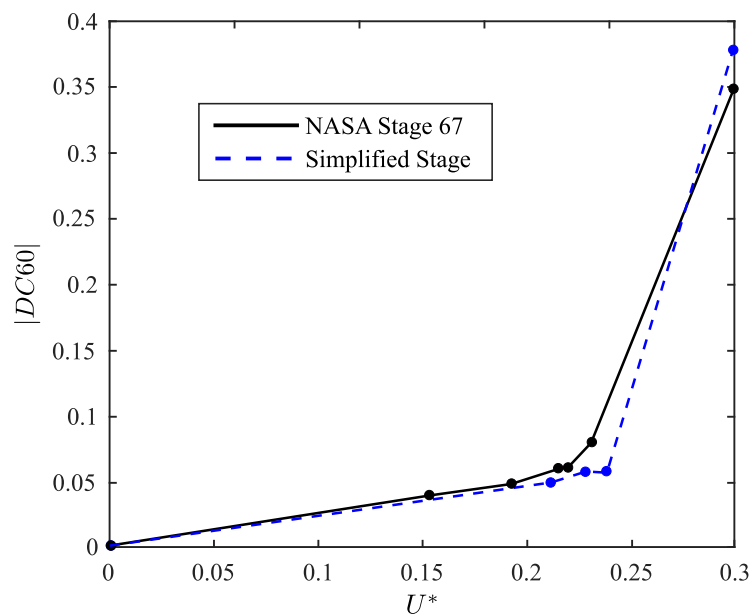


**Figure 15.**  $DC60$  comparison between NASA Stage 67 and the simplified stage as crosswind velocity varies.

The largest difference in the  $DC60$  prediction between the two stages occurred at  $U^* = 0.30$  where the simplified stage over-predicted  $DC60$  by 9%. The simplified stage had a greater rise in  $DC60$  magnitude when  $U^* = 0.30$  due to the circumferential thickness of the separated region. Although the simplified stage under-predicted the maximum decrease in stagnation pressure at the fan face, as well as the axial length of the separated region, the increase in circumferential extent of the separated region caused the area averaged stagnation pressure of the  $60^\circ$  sector to decrease, which led to the higher  $DC60$  magnitude. Figure 15 shows that the effect of stage simplification on the prediction of  $DC60$  was minor over a wide range of  $U^*$  with the only major difference being that the larger crosswind separation velocity caused the sharp increase in  $DC60$  to be delayed by  $U^* = 0.01$ .

## 5. Summary and Conclusions

In this paper, the simplified fan stage gas path and body force model design approach described in Part 1 [6] were applied to predict crosswind separation velocities, as well as the associated effects on fan and nacelle performance. A stage based on NASA Stage 67 was generated. A comparison between this simplified stage and NASA Stage 67 was done with uniform inflow. The simplified stage produced a 1.14% higher  $FPR$  and approximately a 5% difference in the other variables of interest, such as the thrust and overall work coefficient. The stage produced did not match the desired performance as closely as the example fan stage created in Part 1 due to the increase in gas path complexity. It nevertheless allowed for the effects of simplifying the stage to be seen and provided a foundation for investigating non-uniform inflow without detailed stage information.

The intended use for the process described in Part 1 [6] is to allow for assessing external flow–fan interactions when limited fan information is available. This is useful, for example, when airframers wish to investigate coupling between non-uniform inflows caused by off-design operation and the fan. The simplified stage and the original NASA Stage 67 were inserted into a nacelle. Both stages were run in full wheel body force simulations with varying crosswind speeds. The results were compared, and the impacts of simplifying the stage design were investigated. The simplified stage was able to predict the separation velocity to within  $5.1 \pm 1.6\%$ . The Mach number in the crosswind plane was examined, and although the height and width of the recirculation region decreased in the simplified stage, the overall flow showed the same trends. Flow at the fan leading edge was

reproduced well, with the minimum fan stagnation pressure and its location varying by 3.4% and 5.8% respectively between the two stages. The simplified stage can estimate the effect of non-uniformities on the fan, as it captured the maximum change in incidence angle to within  $4.8^\circ$ . To measure the nacelle performance, the  $DC60$  metric was used; the simplified stage showed a maximum difference in  $DC60$  when  $U^* = 0.30$ , with an increase of 9%.

The intended level of fidelity of this process was such that it could be used for early design stages or in the case where no detailed geometry is available; the quantities examined in this paper showed that the simplified stage was capable of reproducing the overall flow found when detailed geometry was used. We showed that the simplified fan model worked well despite changes in blade shape and rotational speed compared to Stage 67. This supports the utility of the approach since the simplified model was intended to be used when the fan rotational speed may not be known. The results also suggested that this process would work under other non-uniform inflow conditions, for example a nacelle with forward movement at the angle of attack. With an angle of attack,  $U^*$  would be larger when separation occurred, and the simplified stage reproduced the flow more accurately before the flow separated, meaning that the case modelled in this paper, pure crosswind, was one of the most challenging scenarios possible for assessing the fan–nacelle interaction. The goodness of agreement obtained despite the significant differences in the fan geometries suggested that an even simpler fan model may in some cases be adequate for capturing fan–nacelle interaction. Determining exactly what the limits are for good agreement is beyond the scope of this paper, but may be an interesting topic for future research.

**Author Contributions:** Conceptualization, Q.J.M. and J.J.D.; data curation, Q.J.M.; formal analysis, Q.J.M.; funding acquisition, J.J.D.; investigation, Q.J.M.; methodology, Q.J.M. and J.J.D.; project administration, J.J.D.; resources, J.J.D.; software, Q.J.M.; supervision, J.J.D.; validation, Q.J.M.; visualization, Q.J.M.; writing, original draft, Q.J.M.; writing, review and editing, J.J.D.

**Funding:** This research and the APC were funded by Bombardier Aerospace, Pratt & Whitney Canada, and the Consortium for Aerospace Research and Innovation in Canada (CARIC), project COMP-1602\_TRL4+.

**Acknowledgments:** Computational resources were provided by the facilities of the Shared Hierarchical Academic Research Computing Network (SHARCNET) ([www.sharcnet.ca](http://www.sharcnet.ca)) and Compute/Calcul Canada ([www.computecanada.ca](http://www.computecanada.ca)). The authors would like to thank Ewan Gunn for the stage 67 stator model used in this work. The authors would also like to thank Bombardier Aerospace for providing the generic nacelle geometry used in this work.

**Conflicts of Interest:** The authors declare no conflict of interest. The funders had no role in the design of the study; in the collection, analyses, or interpretation of data; nor in the writing of the manuscript. The funders approved the publication of the results.

## Abbreviations

The following abbreviations are used in this manuscript:

### Symbols

$A$	Area
$a$	Location of maximum camber
$B$	Number of blades in a row
$b$	Blade span
$c$	Blade chord
$c_p$	Pressure coefficient
$DC60$	Distortion coefficient based on 60°-sector
$e$	Energy
$F$	Thrust
$f$	Force
$h$	Enthalpy
$i$	Incidence angle
$K, K'$	Compressibility correction
$L$	Length
$M$	Mach number
$\dot{m}$	Mass flow rate
$\hat{n}$	Blade camber surface normal unit vector
$p$	Pressure
$R$	Gas constant
$r$	Radius
$s$	Spacing between blades
$T$	Temperature
$U$	Blade speed
$U^*$	Velocity ratio
$\vec{V}$	Velocity
$\vec{W}$	Relative velocity

$\alpha$	Absolute flow angle
$\gamma$	Specific heat ratio
$\delta$	Deviation
$\eta$	Efficiency
$\xi$	Change in blade angle
$\rho$	Density
$\tau$	Shear stress
$Y$	Tip radius change parameter
$\phi$	Flow coefficient
$\psi$	Work coefficient
$\psi_{pt}$	Stagnation pressure rise coefficient
$\omega$	Angular velocity

### Subscripts

i	Incompressible
LE	Blade leading edge
m	Meridional component
mid	Midspan location
R	Rotor
S	Stator
TE	Blade trailing edge
t	Stagnation quantity
x	Axial component
y	Crosswind direction quantity
2	Fan face quantity
13	Fan trailing edge quantity
19	Nozzle exit quantity
$\theta$	Tangential component
$\infty$	Freestream quantity

### Abbreviations

RANS	Reynold averaged Navier–Stokes
RMS	Root mean squared
FPR	Fan stagnation pressure ratio

### References

- Peters, A.; Spakovszky, Z.S.; Lord, W.K.; Rose, B. Ultrashort Nacelles for Low Fan Pressure Ratio Propulsors. *J. Turbomach.* **2015**, *137*, 021001, doi:10.1115/1.4028235.
- Gunn, E.J.; Hall, C.A. Aerodynamics of Boundary Layer Ingesting Fans. In Proceedings of the ASME Turbo Expo 2014, Dusseldorf, Germany, 16–20 June 2014. doi:10.1115/GT2014-26142.
- Fidalgo, V.; Hall, C.; Colin, Y. A Study of Fan-Distortion Interaction Within the NASA Rotor 67 Transonic Stage. *J. Turbomach.* **2012**, *134*, 051011, doi:10.1115/1.4003850.
- Godard, B.; Jaeghere, E.; Nasr, N.; Marty, J.; Barrier, R.; Gourdain, N. Methodologies for Turbofan Inlet Aerodynamics Prediction. In Proceedings of the 35th AIAA Applied Aerodynamics Conference, Denver, CO, USA, 5–9 June 2017. doi:10.2514/6.2017-3413.
- Burlot, A.; Sartor, F.; Vergez, M.; Méheut, M.; Barrier, R. Method Comparison for Fan Performance in Short Intake Nacelle. In Proceedings of the 2018 Applied Aerodynamics Conference, Atlanta, GA, USA, 25–29 June 2018. doi:10.2514/6.2018-4204.
- Minaker, Q.; Defoe, J. Prediction of Crosswind Separation Velocity for Fan and Nacelle Systems Using Body Force Models: Part 1: Fan Body Force Model Generation Without Detailed Stage Geometry. *Int. J. Turbomach. Propuls. Power* **2019**. in press.
- Hall, D.; Greitzer, E.; Tan, C. Analysis of Fan Stage Conceptual Design Attributes for Boundary Layer Ingestion. *J. Turbomach.* **2017**, *139*, 071012, doi:10.1115/1.4035631.
- Yeung, A.; Vadlamani, N.R.; Hynes, T. Quasi 3D Nacelle Design to Simulate Crosswind Flows: Merits and Challenges. *Int. J. Turbomach. Propuls. Power* **2019**, *3*, 25, doi:10.3390/ijtp4030025.

9. Lee, K.; Wilson, M.; Vahdati, M. Effects of Inlet Disturbances on Fan Stability. In Proceeding of the ASME Turbo Expo 2018, Oslo, Norway, 11–15 June 2018. doi:10.1115/1.4042204.
10. Strazisar, A.; Wood, J.; Hathaway, M.D.; Suder, K. *Laser Anemometer Measurements in a Transonic Axial-Flow Fan Rotor*; Techreport 2879; NASA: Washington, DC, USA, 1989.
11. ANSYS Inc. *ANSYS v18.2 User's Guide*; ANSYS Inc.: Canonsburg, PA, USA, 2017.
12. Pointwise. *Pointwise v18.0R4 User's Manual*; Pointwise: Forth Worth, TX, USA, 2017.
13. Roache, P. *Fundamentals of Computational Fluid Dynamics*; Hermosa Publishers: Socorro, NM, USA, 1998.



© 2019 by the authors. Licensee MDPI, Basel, Switzerland. This article is an open access article distributed under the terms and conditions of the Creative Commons Attribution (CC BY-NC-ND) license (<https://creativecommons.org/licenses/by-nc-nd/4.0/>).